Identification of viscoelastic material properties by ultrasonic angular measurements in double through-transmission

Anne-Sophie Poudrel, Max Gattin, Giuseppe Rosi, Marc Rébillat, Jorge Peixinho, Nicolas Bochud, Pierre Margerit

To cite this version:

Anne-Sophie Poudrel, Max Gattin, Giuseppe Rosi, Marc Rébillat, Jorge Peixinho, et al.. Identification of viscoelastic material properties by ultrasonic angular measurements in double through-transmission. Journal of the Acoustical Society of America, 2024, 156 (1), pp.463-474. 10.1121/10.0026518 . hal-04447269

HAL Id: hal-04447269

https://hal.science/hal-04447269v1

Submitted on 8 Feb 2024

Identification of viscoelastic material properties by ultrasonic angular measurements in double through-transmission

A-S. Poudrel[a], M. Gattin[b], G. Rosi[b], M. Rébillat[a], J. Peixinho[a], N. Bochud[b], P. Margerit[a]

[a] *Arts et Métiers Institute of Technology, CNRS, CNAM, PIMM, HESAM Université, Paris, France*
[b] *Univ Paris Est Creteil, Univ Gustave Eiffel, CNRS, UMR 8208, MSME, F-94010 Créteil, France*

Abstract

Recent advances in additive manufacturing of viscoelastic materials have paved the way towards the design of increasingly complex structures. In particular, emerging biomedical applications in acoustics involve structures with periodic micro-architectures, which require a precise knowledge of both longitudinal and transverse bulk properties of the constituent materials. However, the identification of the transverse properties of highly soft and attenuating materials remains particularly challenging. Thereby, the present work provides a methodological framework to identify the frequency-dependent ultrasound characteristics (*i.e.*, phase velocity and attenuation) of viscoelastic materials. The proposed approach relies on an inverse procedure based on angular measurements achieved in double through-transmission, referred as θ-scan. Towards this goal, a forward modeling of the double transmitted waves through a homogeneous solid is proposed for any incidence angle based on the global matrix formalism. The experimental validation is conducted by performing ultrasound measurements on two types of photopolymers commonly employed for additive manufacturing purposes: a soft elastomer (Elastico™Black) and a glassy polymer (VeroUltra™White). As a result, the inferred dispersive ultrasound characteristics are of interest for the computational calibration and validation of models involving complex multi-material structures in the MHz regime.

Keywords: viscoelasticity, transverse properties, photopolymer material, global matrix formalism, inverse problem.

---

1. Introduction

Additive manufacturing (AM), also referred to as 3D printing, has increasingly expanded over the past decade in engineering and sciences. The development of accurate and versatile 3D printing technologies has paved the way to the design of customized and complex structures printed with a large choice of materials, ranging from elastomers and polymers to ceramics or metals [1, 2]. Among these, multi-material jetting, also known as inkjet technology, represents a powerful multi-material 3D printing process, which allows tailoring the material composition from the micro to the macro scale. For instance, this process has not only enabled the fabrication of heterogeneous materials with dissimilar properties [3], such as periodic lattices or porous media [4], but also interpenetrating phase composites [5] or functionally graded materials [6, 7].

In this context, multi-material photopolymer-based AM has experienced a significant interest in acoustics to design and fabricate tailored tissue-mimicking phantoms [8] for calibrating ultrasound imaging systems [9, 10] or for therapeutic ultrasound applications [11]. Interestingly, the achievement of controlled bio-inspired structures involving periodic micro-architectures has also experienced recent advances to design scaffolds for bone tissue repair [12]. As the prediction of the acoustic behavior of such structures is particularly challenging, recent modeling efforts have focused on disentangling the relative contributions of viscoelasticity and periodicity on ultrasonic signatures, such as dispersion, attenuation, and bandgaps localization [13, 14]. In this respect, an accurate identification of both longitudinal and transverse ultrasound characteristics (*i.e.*, phase velocity and attenuation) of the constituent phases is typically required, together with their frequency dependence.

Notwithstanding, while several ultrasound characterization methods have been explored to measure longitudinal bulk properties of photopolymer materials, including broadband reflection and transmission techniques [9, 15, 10] only a limited number of works have been carried out to report on their transverse properties [16]. Interestingly, the latter study, which relies on the double through-transmission technique, exploits mode conversion at the liquid-solid interface in oblique incidence in order to measure the transverse properties of the wave propagating inside the material. This approach has been initially developed to measure the phase velocity of anisotropic elastic materials [17, 18] and was then extended to the measurement of the attenuation of viscoelastic materials [19]. Although this technique has the advantage to provide longitudinal and transverse bulk properties on a broad frequency range by windowing four measured echoes only (*i.e.*, front-face and back-face reflections at normal incidence, double through-transmission at normal and oblique incidences), it suffers from several drawbacks. First, the frequency-thickness product of the sample must be optimized to ensure a proper temporal separation of the echoes. Second, the identification of the transverse bulk properties relies on a measurement performed after the critical angle, above which only transverse waves propagate through the sample. In the case of soft and highly attenuating materials, the critical angle is high, and so the propagation distance is large, as a consequence of which the transverse wave retrieved in double through-transmission is typically drown in noise. Altogether, these limitations prevent straightforwardly applying the approach described in Gattin et al. [16] to highly viscoelastic materials.

Alternatively, another approach to retrieve the bulk properties of viscoelastic samples relies on the analysis of the reflection and transmission coefficients obtained for different incident angles in simple transmission [20]. An optimization process, performed on the measurement of these coefficients and their modeled counterparts [21, 22], then allows retrieving apparent longitudinal and transverse properties. This approach has been widely applied to anisotropic and viscoelastic materials [23, 24] and has also been recently extended to evaluate the anisotropy of adhesive bonds [25]. Unlike for the *classical* double through-transmission technique, no temporal separation of the echoes is needed here. However, the application of this approach to highly viscoelastic materials is not straightforward since the previous studies have not considered dispersive properties. Moreover, only the amplitude of the transmission and refection coefficients was used in the optimization process, thereby neglecting their phases, which may also carry information on the bulk properties.

Here, we propose to leverage the methodology initially introduced by Castaings et al. [20] on composites, together with the advantages of the double through-transmission technique [16], to estimate the ultrasound characteristics of photopolymer materials. In particular, the purpose of this work is to provide a methodological framework towards the identification of the frequency-dependent bulk properties of highly viscoelastic materials, without the need to isolate the transverse waves after the critical angle. The originality of this work not only lies in the estimation of the longitudinal and transverse phase velocities and attenuations of photopolymer materials, but also of their frequency-dependence, as well as the thickness of the sample, by considering the complex transmission transfer function in the optimization process. To validate our approach, ultrasound measurements were performed in double through-transmission on viscoelastic samples manufactured using a multi-material 3D printing technology. To this end, several combinations of two dissimilar photopolymers –a glassy polymer and a soft elastomer– were investigated.

The remainder of the paper is organized as follows: Sec. 2 describes the additively manufactured samples along with the experimental setup used to achieve the angular measurements in double trough-transmission. Then, Sec. 3 states the principle of the double through-transmission modeling at normal and oblique incidence according to the global matrix formalism, considering both the wave amplitude and phase. The optimization strategy for material properties identification is detailed in Sec. 4. Eventually, the ultrasound characteristics of the photopolymer materials and, in particular, the influence of the volume fraction of each of the two studied materials are reported and discussed in Sec. 5.

2. Experimental method

The proposed ultrasound characterization method relies on the measurement of double through-transmitted signals across the samples at various incident angles, as schematically depicted in Fig. 1. This angular measurement will be referred as *angular scan* in what follows, and its time representation will be named θ-scan.

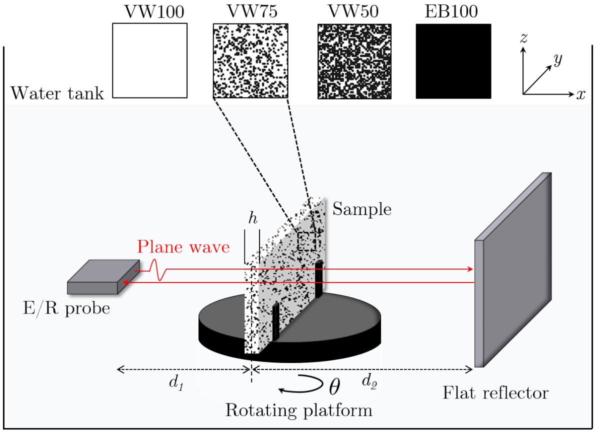

Figure 1: Schematic representation of the experimental setup used for measuring double through-transmitted signals at various incident angles, *i.e.*, $0° \leq \theta \leq 64°$, on photopolymer samples made of VeroUltra™White (VW) and Elastico™Black (EB).

2.1. Additively manufactured samples

Multi-material photopolymer samples were achieved using a commercial 3D printer (Polyjet Pro J35, Stratasys, Los Angeles, CA). This additive manufacturing technology consists in projecting multiple drops of UV-curable photopolymer on a building tray through printing nozzles according to a layer-by-layer process [26]. At the microscopic scale (*i.e.*, voxel resolution around 18 μm), this inkjet technology allows for the mixing of photopolymers with highly dissimilar viscoelastic properties thanks to the concurrent spreading of multiple streams. At the macroscopic level (*i.e.*, millimetric wavelength in the ultrasound regime), this process results in quasi-homogeneous materials obtained by randomly mixing two contrasted photopolymers.

In this study, two photopolymers were employed: a rigid glassy polymer (commercial name: VeroUltra™White, denoted by VW) and a soft elastomer (commercial name: Elastico™Black, denoted by EB). The two pure materials were investigated, 100% of VW (VW100) and 100% of EB (EB100), together with two intermediate volume fractions V_f of VeroUltraWhite, 75% (VW75) and 50% (VW50). The samples were manufactured according to a rectangular plate geometry with overall dimensions of $35 \times 90 \times h$ mm^3. The length and the width of the samples were selected so that they cover the probe emission surface (recall

Fig. 1). The thickness h ranged between 2.5 and 4 mm to ensure a sufficient double through-transmission across the sample for all measurements below the critical angle [27], that is to avoid a too low signal-to-noise ratio (SNR) for the transverse waves because of the attenuation. Note that one sample was manufactured for each material, except for the VW100, for which two samples with two different thicknesses were tested: $h = 4$ mm (VW100) and $h = 2.7$ mm (VW100$_t$). The mass density ρ of each sample was determined from their mass measured with an electronic balance (± 0.01 mg) and their dimensions measured with a caliper (± 0.02 mm).

2.2. Experimental setup

All measurements were carried out using a multielement probe (Imasonic SAS, Voray sur l'Ognon, France) driven by a programmable multi-channel electronics (Advanced OEM Solutions, WestChester, USA). First developed for medical imaging applications (*e.g.*, elastography [28]), this type of device was recently used to characterize the bulk properties of both homogeneous [16] and heterogeneous photopolymer samples [15, 13] in the MHz regime. Measurements were performed using a linear transducer array that consists of 32 elements. Each element had a width and a height of 0.5 and 12 mm, respectively, leading to a total transmission surface of 16×12 mm^2. The transducer operated at a central frequency $f_c = 2.25$ MHz (–6 dB frequency bandwidth from 1.5 to 3 MHz) and the pitch of the array was 0.5 mm.

As schematized in Fig. 1, measurements were carried out in a water tank at room temperature (22 ± 0.5 °C) using a plane wave imaging mode, by concurrently emitting a pulse on all elements. The water temperature was controlled by a digital thermometer throughout the experiments (Zacro LCD digital thermometer, resolution of ±0.1 °C), so that the water celerity could be estimated using Marczak's polynomial model [29]. The received signals $s(t)$ were recorded during 150 μs starting from 300 μs after the pulse emission to target double-through transmitted waves only, using a sampling rate of 100 MHz and 12-bit resolution. The advantages of using a multielement probe both as emitter and receiver rather than a monoelement one are here twofold. First, as the wavelength in water at the central frequency was small compared to the lateral dimension of the probe array, a high directivity factor was assumed, and thus geometrical diffraction effects could be neglected in the further processing and modeling of the double through-transmitted signals. Second, the recorded signals could be averaged over the 32 elements of the probe, thus enhancing the SNR of the measurement [16]. To retrieve double through-transmitted waves, a large flat reflector was used, which was oriented parallel to the transducer. In this configuration, the backward propagating plane waves travel exactly along the same path as the forward incident wave [18]. Thereby, the transducer remains fixed, regardless of the incident angle, whereas in simple through-transmission the receiver has to be shifted

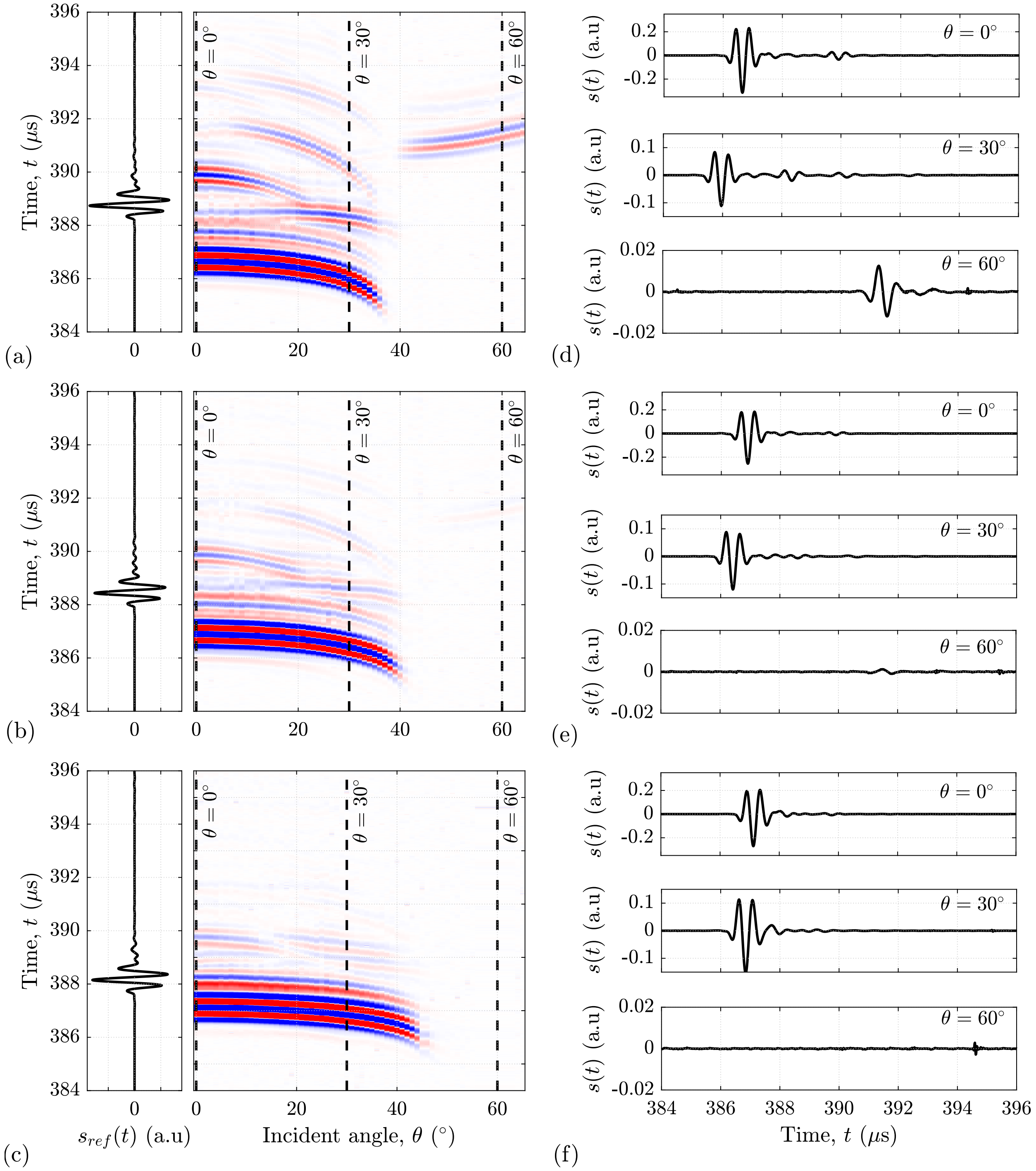

Figure 2: Examples of experimental θ-scans of double through-transmitted signals measured on (a) VW100, (b) VW50, and (c) EB100 samples, along with their respective signal displacements $s(t)$ ((d), (e) and (f), respectively) obtained at three specific incident angles $\theta = 0°$, $30°$ and $60°$. The saturated colormap for each θ-scan represents the normalized positive (in red) and negative (in blue) amplitude of the signals. The double through-transmitted signal measured in water only, denoted by $\tilde{s}_{\mathrm{ref}}(t)$, is also shown for comparison.

depending on the angle of the incident wave [20, 17]. Another advantage of double through-transmission is to reduce the amplitude differences between the different waves being compared, which is of paramount importance for transverse wave measurement in highly attenuating materials, where this amplitude difference could be in the same order of magnitude than the dynamic range of the transducer, leading to weak SNR or signal distortion.

The samples were mounted on a motorized rotation stage ($\pm 1^\circ$) and the signals $s(t)$ were recorded for each incident angle θ between 0° and 64° with a 1° step. Note that the maximal incident angle was chosen to ensure that the probe emission surface was still entirely aiming the sample. Eventually, the double through-transmitted wave across the water only, denoted by $s_{\mathrm{ref}}(t)$, was measured by removing the sample, without moving the transducer and the flat reflector. To evaluate the reproducibility of the measurement (*e.g.*, probe-sample-mirror alignment, parallelism of the sample's faces), the full *angular scan* measurement was repeated three times on the VW100 sample.

Three examples of experimental θ-scans are shown in Fig. 2 for the following materials: (a) VW100, (b) VW50, and (c) EB100, together with the temporal signals $s(t)$ obtained at three specific incident angles, *i.e.*, $\theta = 0^\circ, 30^\circ$ and 60°. As can be observed, the critical angle is visible on each θ-scan at the angle for which the signal vanishes, and its value increases when the volume fraction of VW decreases. In addition, while the transverse wave is clearly visible after the critical angle for the VW100 sample (see Fig. 2(a) and (d) at $\theta = 60^\circ$), its amplitude is much lower for the VW50 sample (see Fig. 2(b) and (e) at $\theta = 60^\circ$) and totally drown in noise for the EB100 sample (see Fig. 2(c) and (f) at $\theta = 60^\circ$). These observations overall support the need of a specific methodology to retrieve the transverse properties of such attenuating materials.

3. Double through-transmission modeling

We consider the double through-transmission (forward path, reflection on a mirror then backward path [18]) of a plane harmonic acoustic wave with angular frequency ω and incidence angle θ through an homogeneous and isotropic solid material (mass density ρ, longitudinal and transverse wave numbers k_ℓ and k_t, respectively) immersed in a fluid (mass density ρ_0, wave number k_0). The mirror surface is assumed to be normal to the acoustic wave vector $\boldsymbol{k}_0 = k_0\,[\cos\theta\ \sin\theta]$, so that the forward and backward paths are *symmetrical.*

The method relies on the relation between the double through-transmitted signals measured *with* the sample inserted and *without* it (so-called insertion/substitution method [30]). These are respectively denoted by $S(\omega)$ and $S_{\mathrm{ref}}(\omega)$ as the Fourier coefficients of $s(t)$ and $s_{\mathrm{ref}}(t)$ at the frequency ω. Dropping the dependence of all variables on ω, such relation can be expressed as

$$S = H_{\mathtt{T}}^2\, S_{\mathrm{ref}}\ , \tag{1}$$

where

$$S_{\mathrm{ref}} = S_{\mathrm{in}}\ \overbrace{P(d_1+d_2)}^{\text{forward}}\ \underbrace{R}_{\text{reflection}}\ \overbrace{P(d_2+d_1)}^{\text{backward}} \tag{2}$$

and

$$S = S_{\mathrm{in}}\ \overbrace{P(d_1)\ \underbrace{H_{\mathtt{T}}}_{\text{transmission}}\ P(d_2)}^{\text{forward}}\ \underbrace{R}_{\text{reflection}}\ \overbrace{P(d_2)\ \underbrace{H_{\mathtt{T}}}_{\text{transmission}}\ P(d_1)}^{\text{backward}}\ , \tag{3}$$

where S_{in} is the complex spectrum of the input signal, $P(d_i) = e^{-\mathrm{i}k_0 d_i}$ is the propagation *phase* associated with the fluid path d_i, with $i = 1, 2$, R is the transfer function associated with the reflection on the mirror, and $H_{\mathtt{T}}$ is the transfer function corresponding to the *single* transmission of waves through the specimen. The distances d_1 and d_2 respectively correspond to the probe-sample and sample-mirror distances, as shown in Fig. 1. These are defined with respect to *the plane of symmetry of the sample*, so that $H_{\mathtt{T}}$ already takes into account the phase $P(-h)$ associated with the insertion of the sample in the propagating path.

It is thus clear that measuring the reference signal $s_{\mathrm{ref}}(t)$ presents several advantages: the transfer function $H_{\mathtt{T}}$ can be estimated experimentally and used as the basis for the identification of the sample properties without prior knowledge of the distances d_1 and d_2, the input signal S_{in} and, more interestingly, the mirror reflection transfer function R. Hence, the mirror can be of arbitrary material and/or thickness [17], without constraint associated with the time separation of the successive trains of echoes.

3.1. Single transmission transfer function

As the relation between S and S_{ref} only involves the squared transfer function $H_{\mathtt{T}}$, the model of the experimental data is reduced to the calculation of the *single wave transmission* that corresponds to the problem statement shown in Fig. 3. We thus derive here $H_{\mathtt{T}}$ as the ratio between the transmitted and incident complex wave amplitudes, respectively denoted by $a_{\mathtt{T}}$ and $a_{\mathtt{I}}$, for any incident angle θ and frequency ω. The 2D coordinate system (x, y) is chosen so that the two infinite solid–fluid plane interfaces are situated at $x = \pm h/2$ and their normal is along x. Hence, all wave phases are expressed *with respect* to the solid layer plane of symmetry at $x = 0$.

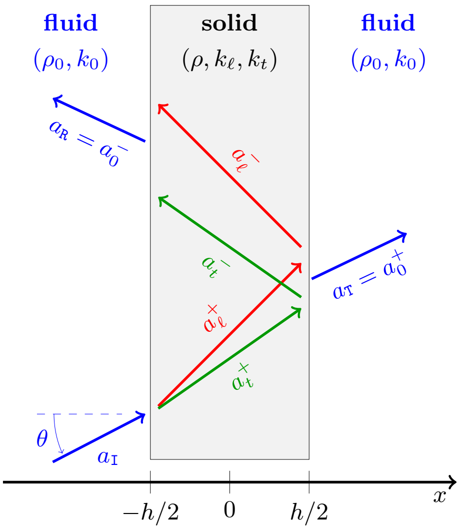

Figure 3: Scheme of the single wave transmission problem.

In each subdomain, the pressure field p or displacement field $\boldsymbol{u}$ is assumed as a combination of plane waves with amplitudes a_r, polarizations $\mathcal{P}^{(r)}$ or $\boldsymbol{\mathcal{U}}^{(r)}$ and wavevector $\boldsymbol{k}_r = [\xi_r \ \kappa_r] = k_r[\cos\theta_r \ \sin\theta_r]$ as

$$\begin{bmatrix} \boldsymbol{u}(x,y) \\ p(x,y) \end{bmatrix} = \sum_r a_r \begin{bmatrix} \boldsymbol{\mathcal{U}}^{(r)} \\ \mathcal{P}^{(r)} \end{bmatrix} e^{-\mathrm{i}(\xi_r x + \kappa_r y)} \ , \tag{4}$$

with r standing either for the wave propagating in water ($r = 0$) or the *longitudinal* ($r = \ell$) and *transverse* ($r = t$) waves in the solid.

The relation between wave amplitudes is governed by the continuity of the stress vector and normal displacements at both solid–fluid interfaces, which can be expressed as

$$\sigma_{xx}(x = \pm\frac{h}{2}, y) + p(x = \pm\frac{h}{2}, y) = 0 \ , \tag{5a}$$

$$\sigma_{xy}(x = \pm\frac{h}{2}, y) = 0 \ , \tag{5b}$$

$$\rho_0\omega^2 u_x(x = \pm\frac{h}{2}, y) - \frac{\partial}{\partial x} p(x = \pm\frac{h}{2}, y) = 0 \ . \tag{5c}$$

As these 6 continuity equations need to be fulfilled for any y, the wave modulation $e^{-\mathrm{i}\kappa_r y}$ along the vertical axis must be constant across interfaces. This leads to the well-known Snell-Descartes law as

$$\kappa_r = k_r \ \sin\theta_r = k_0 \ \sin\theta = \kappa \ , \ \forall r \tag{6}$$

where κ is the *vertical* component of the wavevector that is a constant of the problem. It is worth noting that the wavevectors $\boldsymbol{k}_r$ are generally complex and can have non-colinear real and imaginary parts; thus, the angles θ_r can take complex values in general. Here it is chosen to derive the following expressions using the wavevector components (ξ_r, κ). In particular, the *absolute* projection χ_r of the wavevectors on the x-axis, such that $\xi_r = \pm\chi_r$, is defined as

$$\chi_r = \sqrt{k_r^2 - \kappa^2}\ , \tag{7}$$

where χ_r may take complex values when $|k_r| < |\kappa|$.

The 6 continuity equations in Eq. 5 can then be recast following a global matrix formalism [31] (see Appendix A). By taking into account the symmetries of the fluid-solid interfaces and of the forward-backward waves, the matrix can be recast to obtain two decoupled 3×3 systems, which can be subsequently analytically inverted to recover the expressions of a_0^S and a_0^A, so that $a_r^{\pm} = a_r^S \pm a_r^A$, where the superscripts A and S stand for antisymmetric and symmetric parts, respectively. At the end, using the fact that $a_{\mathrm{T}} = a_0^+ = a_0^S + a_0^A$, the analytical expression of the complex transfer function associated with the single wave *transmission* H_{T} through the solid domain reads as

$$H_{\mathrm{T}} = \frac{a_{\mathrm{T}}}{a_{\mathrm{I}}} = -4\,\frac{\gamma}{\Pi_0}\,\frac{\alpha\Pi_\ell(\Pi_t^2-1)+\beta\Pi_t(\Pi_\ell^2-1)}{\Delta}\ , \tag{8}$$

where

$$\begin{aligned}
\Delta &= (\alpha+\beta-\gamma)^2\big(\Pi_\ell^2-1\big)\big(\Pi_t^2-1\big)\\
&\quad -4\beta\gamma\big(\Pi_\ell^2-1\big)-4\alpha\gamma\big(\Pi_t^2-1\big)\\
&\quad +4\alpha\beta\big(\Pi_\ell-\Pi_t\big)^2\ ,
\end{aligned} \tag{9a}$$

$$\Pi_r = e^{-\mathrm{i}\chi_r h}\ , \tag{9b}$$

$$\alpha = (\chi_t^2-\kappa^2)^2\ , \tag{9c}$$

$$\beta = 4\kappa^2\chi_\ell\chi_t\ , \tag{9d}$$

$$\gamma = \frac{\rho_0}{\rho}\frac{\chi_\ell}{\chi_0}(\chi_t^2+\kappa^2)^2\ . \tag{9e}$$

3.2. Frequency-dependence of the wave number

The single transmission transfer function H_{T} given by Eq. (8) can be used to compute, from Eq. (1) and the measured reference signal $s_{\mathrm{ref}}(t)$, the θ-scan corresponding to a sample with given wave dispersion characteristics. In other words, the dependence of k_0, k_ℓ and k_t with the frequency ω needs to be provided in order to predict the double through-transmitted signal $s(t)$. In the following, we use the general formulation

$$k_r(\omega) = \frac{\omega}{v_r(\omega)} - \mathrm{i}\,\alpha_r(\omega) \ , \tag{10}$$

where $v_r(\omega)$ and $\alpha_r(\omega)$ respectively denote the phase velocity and attenuation as *real* functions of the frequency.

3.2.1. Non-dispersive media

As a starting point, non-dispersive properties can be assumed for both the solid and the fluid media, characterized with a *complex* and *constant* wave celerity $c_r \in \mathbb{C}$ such that $k_r(\omega) = \omega/c_r$. Hence,

$$v_r(\omega) = \Re(c_r)\left(1 + \frac{\Im(c_r)^2}{\Re(c_r)^2}\right) \quad \text{and} \quad \alpha_r(\omega) = \omega\frac{\Im(c_r)}{|c_r|^2} \ . \tag{11}$$

This assumption is known to provide a good approximation for the wave number k_0 associated with pressure waves in the fluid. In particular, as the temperature is known, the wave celerity c_0 in water can be predicted using Marczak's polynomial model [29]. In this work, the non-dispersive model from Eq. (11) is also used to provide an initialization for the material wave numbers (k_ℓ, k_t) needed in the inverse problem (see Sec 4.1).

3.2.2. Szabo's rheological model

Viscoelastic materials such as photopolymers exhibit dispersive losses that cannot be accurately captured by a classical rheological Voigt model (*i.e.*, attenuation proportional to ω^2), which may be due to their heterogeneous nature involving multiple relaxation mechanisms. Nevertheless, earlier studies by our group [15, 16] evidenced that the viscoelastic behavior of photopolymers may be well described by the Szabo's model [32]. This phenomenological model has the advantage to describe not only the frequency-dependence of the attenuation $\alpha_r(\omega)$ with a power-law, but also the frequency variations of the phase velocity $v_r(\omega)$, because the model is causal in the sense that it satisfies Kramer-Kronig relationships [33]. In this regard, convenient expressions of $v_r(\omega)$ and $\alpha_r(\omega)$ as a function of a reference frequency ω_c, were proposed by Bakaric et al. [10] as

$$v_r(\omega) = \left(\frac{1}{v_{cr}} + \frac{\alpha_{cr}}{\omega_c} \tan\left(\frac{\pi}{2} y_r\right) \left(\left(\frac{\omega}{\omega_c}\right)^{y_r - 1} - 1 \right) \right)^{-1} , \tag{12a}$$

$$\alpha_r(\omega) = \alpha_{cr} \left(\frac{\omega}{\omega_c}\right)^{y_r} , \tag{12b}$$

where $\omega_c = 2\pi f_c$ can be deliberately chosen as the central frequency of the available ultrasonic probe. With the Szabo model, the dependence of the wave number $k_r(\omega)$ with the frequency is thus completely given by the three corresponding parameters v_{cr}, α_{cr} and y_r, which respectively denote the phase velocity and attenuation at the central frequency ω_c and a dispersion coefficient.

4. Identification of viscoelastic material properties

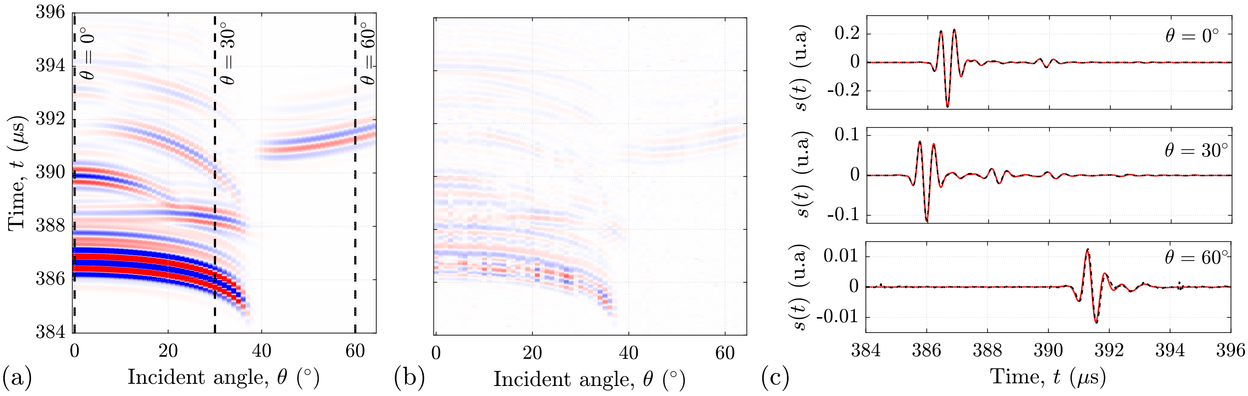

Figure 4: Illustration of the optimization procedure applied to one realization of the VW100 sample: (a) Modeled θ-scan obtained with the optimized set of parameters $\hat{\boldsymbol{p}}$, (b) difference between the experimental θ-scan shown in Fig. 2a and the modeled θ-scan, and (c) comparison of experimental (- - -) and modeled (——) double through-transmitted signals at three specific incident angles $\theta = 0°$, $30°$ and $60°$. The colormaps of (a) and (b) are ten times saturated to highlight the successive echoes arising from the mode conversion at the interfaces.

The inverse procedure used to identify the ultrasound characteristics (phase velocity $v_r(\omega)$ and attenuation $\alpha_r(\omega)$) from a measured θ-scan $s(t,\theta)$, the reference signal $s_{\text{ref}}(t)$ and the model $H_{\text{T}}(\omega,\theta)$ is described in what follows. In practice, the wave dispersion $k_r(\omega)$ needs to be given on the whole frequency domain in order to reconstruct a *candidate* θ-scan using Eq. (1). However, the ultrasound probe is characterized by a *limited* bandwidth around ω_c. Thereby, a rheological model such as Eq. (11) or Eq. (12) is used to regularize the inverse problem. In particular, the procedure is here divided into two steps [34]. First, an initial *guess* is provided using the estimation of a non-dispersive longitudinal celerity c_ℓ via a direct problem. Second, an optimization procedure is implemented to estimate the model parameters of the Szabo model.

4.1. Calibration of the model at normal incidence

For a normally incident plane wave ($\theta = 0$), the vertical component of the wavevector vanishes, thus $\kappa = 0$. Consequently, the expression of H_{T} in Eq. (8) can be simplified to

$$H_{\mathrm{T}} = \frac{T_\ell^2}{\Pi_0} \left(\Pi_\ell^{-1} - R_\ell^2 \, \Pi_\ell \right)^{-1} \ , \tag{13}$$

where

$$T_\ell = \frac{2\zeta_\ell}{\zeta_\ell + 1} \ , \ R_\ell = \frac{\zeta_\ell - 1}{\zeta_\ell + 1} \ , \quad \text{and} \ \zeta_\ell = \frac{\rho}{\rho_0} \frac{k_0}{k_\ell} \ .$$

Under the hypothesis of a *non-dispersive* material behavior (recall Eq. (11)), it is noteworthy that ζ_ℓ, thus T_ℓ and R_ℓ, are constants. In such a case, this allows us to express the inverse of the double through-transmission transfer function as

$$\frac{S_{\mathrm{ref}}(\omega)}{S(\omega)} = \left[H_{\mathrm{T}}(\omega) \right]^{-2} = \frac{\psi_0^\omega}{T_\ell^4} \left(\psi_\ell^{-\omega} - 2R_\ell^2 + R_\ell^4 \, \psi_\ell^\omega \right) \ , \tag{14}$$

where $\psi_r = e^{-\mathrm{i}\frac{2h}{c_r}}$. Once the above expression is multiplied by $\psi_0^{-\omega}$, which can be computed from the wave celerity c_0 in water and the specimen thickness h, it takes the form of an harmonic polynomial in ψ_ℓ only. Hence, a Prony method is implemented here to provide an initial guess of the longitudinal wave number k_ℓ associated with a constant celerity $c_\ell \in \mathbb{C}$ (see Appendix B).

4.2. Estimation of dispersive properties

We propose an optimization procedure based on the full θ-scan, to identify, for each sample, the parameters of the Szabo model (recall Eq. (12)), *i.e.*, $\boldsymbol{p}_r = [v_{cr}, \alpha_{cr}]$ associated with longitudinal ($r = \ell$) and transverse ($r = t$) waves. Note that the dispersion coefficient y_r involved in Szabo's model is assumed to be equal to $y_\ell = 1.1$ and $y_t = 0.7$ for all the investigated materials, based on the results obtained in [15, 16]. In addition, the sample thickness h and a uniform angle correction θ_0, which may be interpreted as an experimental angle offset at the normal incidence, are included as *refinement* parameters in order to avoid biases due to their experimental initial determination. The set of parameters $\boldsymbol{p} = [\boldsymbol{p}_\ell, \boldsymbol{p}_t]$ is thus estimated via the following minimization problem:

$$(\hat{\boldsymbol{p}}, \hat{h}, \hat{\theta_0}) = \underset{\substack{\boldsymbol{p} \in \mathbb{R}^4 \\ h \in \mathbb{R} \\ \theta_0 \in \mathbb{R}}}{\arg\min} \sum_{t_i, \theta_j} \Delta s(t_i, \theta_j; \boldsymbol{p}, h, \theta_0)^2 \tag{15}$$

with the residual Δs given by:

$$\Delta s(t, \theta; \boldsymbol{p}, h, \theta_0) = u(t, \theta; \boldsymbol{p}, h, \theta_0) - s(t, \theta) \tag{16}$$

and the signal *model* u computed as:

$$u(t, \theta; \boldsymbol{p}, h, \theta_0) = \mathcal{F}^{-1}\left[H_{\mathrm{T}}(\omega, \theta + \theta_0; \boldsymbol{p}, h)\ S_{\mathrm{ref}}(\omega)\right] \tag{17}$$

where $\mathcal{F}^{-1}$ denotes the inverse Fourier Transform. In contrast to an estimation that would be based on the transfer function only, performing the minimization directly on the temporal data $s(t, \theta)$ provides a natural *weighting* of the error, associated with the reference signal s_{ref}, that accounts both for the probe's bandwidth and losses/reflections in the mirror.

The optimization procedure was implemented using a gradient-based method implemented in Matlab (The MathWorks Inc., Natick, MA) and finite differences for the numerical estimation of the gradient of the residuals.

As required by such approach, a specific initialization of the set of model parameters $\boldsymbol{p}$ was performed. The longitudinal parameters of the Szabo model $\boldsymbol{p}_\ell$ were initialized from the longitudinal wave number k_ℓ, which is associated with the constant complex velocity c_ℓ estimated at the normal incidence using the model calibration described in Sec. 4.1. Likewise, the initialization of the transverse parameters $\boldsymbol{p}_t$ was subsequently determined from the complex transverse wave celerity c_t, which can be determined from the relation

$$c_t = c_\ell \sqrt{\frac{1 - 2\nu_{\mathrm{i}}}{2(1 - \nu_{\mathrm{i}})}}\ , \tag{18}$$

assuming an *initial* Poisson's ratio ν_{i} equal to 0.38 for all samples [16]. Eventually, the angle correction θ_0 was arbitrary initialized to 0.01°, which corresponds to the uncertainty of the rotating platform and the sample thickness h was initialized to the experimental value measured with a caliper, as described in Sec. 2.

To serve as an example, Fig. 4 depicts the optimal matching between the measured and modeled θ-scans for the VW100 sample. As can be observed, the measured and modeled signals are in excellent agreement, which is shown herein for three specific incidence angles θ.

4.3. Uncertainty of the identification procedure

The uncertainty associated with the inverse procedure, noted $\boldsymbol{\sigma}_{\hat{\boldsymbol{p}}}$, was evaluated via error propagation for the set of parameter $\hat{\boldsymbol{p}}$, assuming independent variables, as

$$\sigma_{\hat{p}_k} = \sqrt{\sum_{t_i,\theta_j} \left(\left. \frac{\partial p_k}{\partial u} \right|_{(t_i,\theta_j;\hat{\boldsymbol{p}},\hat{h},\hat{\theta}_0)} \right)^2 \Delta s(t_i,\theta_j;\hat{\boldsymbol{p}},\hat{h},\hat{\theta}_0)^2} \;, \tag{19}$$

where the terms between parentheses are obtained via an inversion of the model sensitivity matrix. At the end, each parameter is associated to a confidence interval of 95% such that $p_k \pm 1.96\,\sigma_{\hat{p}_k}$.

5. Results

The optimized Szabo's parameters $\boldsymbol{p}_r = [v_{cr}, \alpha_{cr}]$, for $r = \{\ell, t\}$, are reported in Table 1 for all samples, together with the optimized sample thickness $\hat{h}$ and the uniform incident angle correction $\hat{\theta}_0$. All values are given with their respective uncertainty, which is related to the identification procedure as explained in Sec. 4.3.

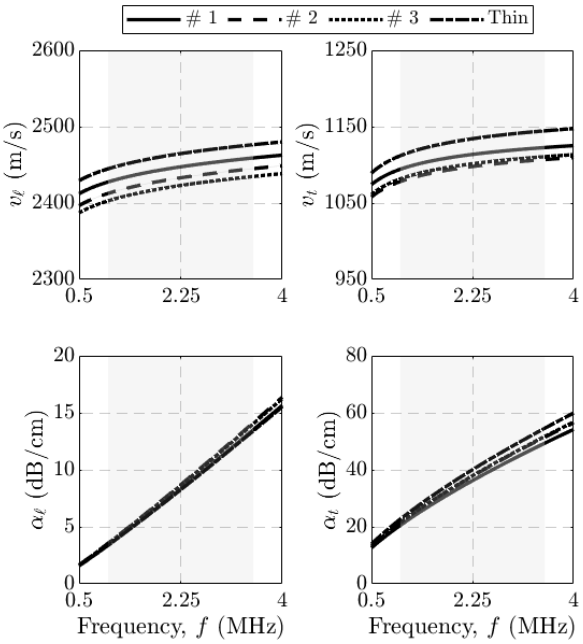

Figure 5: Ultrasound characteristics, *i.e.* the phase velocity $v_r(\omega)$ and the attenuation $\alpha_r(\omega)$, obtained for three measurements performed on the VW100 sample. The light gray areas display the useful frequency bandwidth of the probe on which the inversion was conducted.

5.1. *Measurement reproducibility*

The ultrasound characteristics of VW are shown in Fig. 5 for three independent measurements performed on the same sample, along with a measurement performed on a thinner sample.

On the onde hand, at the probe's central frequency, *i.e.*, $f_c = 2.25$ MHz, some discrepancies can be observed across the three measurement repetitions. While the optimized longitudinal phase velocity $\hat{v}_{c\ell}$ varies between 2423.0 ± 0.5 m/s and 2447.4±0.2 m/s, the transverse phase velocity $\hat{v}_{ct}$ varies between 1097.9±0.3 m/s and 1113.7±0.1 m/s, which represents less than 2% of relative error. Comparable results are obtained for the attenuation, where the optimized longitudinal attenuation $\hat{\alpha}_{c\ell}$ (respectively transverse attenuation $\hat{\alpha}_{ct}$) ranges between 8.31±0.01 dB/cm and 8.69 ±0.04 dB/cm (respectively between 37.9 ± 0.1 dB/cm and 36.2 ±0.1 dB/cm), which stands for a relative error of about 5%.

On the other hand, although the results obtained on the two samples of VW named as VW100 and VW100$_t$ in Table 1 are in relatively good quantitative agreement, the overall optimized Szabo's parameters $[\boldsymbol{p}_\ell, \boldsymbol{p}_t]$ are slightly higher for the thinner sample. These variations across the samples and the measurements will be further discussed in Sec. 6.

5.2. *Influence of the material mixing*

	ρ (kg/m^3)	Measure #	$\hat{\theta}_0$ (°)	$\hat{h}$ (mm)	r	$\hat{v}_{cr}$ (m/s)	$\hat{\alpha}_{cr}$ (dB/cm)
VW100	1185.3 ± 0.5	1	0.14 ± 0.01	3.98 ± 0.00	ℓ	2447.4 ± 0.2	8.31 ± 0.01
					t	1113.7 ± 0.1	36.2 ± 0.1
		2	0.03 ± 0.03	3.93 ± 0.00	ℓ	2433.1 ± 0.9	8.69 ± 0.04
					t	1097.9 ± 0.3	37.8 ± 0.11
		3	0.28 ± 0.02	3.93 ± 0.00	ℓ	2423.0 ± 0.5	8.63 ± 0.02
					t	1101.5 ± 0.2	37.9 ± 0.1
VW100$_t$	1185.3 ± 0.5	1	0.64 ± 0.07	2.76 ± 0.01	ℓ	2464.7 ± 1.7	8.25 ± 0.11
					t	1134.2 ± 0.4	40.1 ± 0.1
VW75	1162.9 ± 0.4	1	0.01 ± 0.02	3.67 ± 0.00	ℓ	2379.5 ± 0.3	9.50 ± 0.02
					t	1069.1 ± 0.2	47.2 ± 0.2
VW50	1147.9 ± 0.7	1	1.16 ± 0.02	3.39 ± 0.01	ℓ	2255.8 ± 0.6	11.5 ± 0.1
					t	991.4 ± 1.0	69.3 ± 0.8
EB100	1115.1 ± 0.8	1	1.24 ± 0.03	2.78 ± 0.01	ℓ	2035.1 ± 0.9	15.4 ± 0.03
					t	740.6 ± 0.8	86.3 ± 1.5

Table 1: Measured mass density ρ and optimized ultrasound parameters $\hat{\boldsymbol{p}} = [\hat{v}_{cr}, \hat{\alpha}_{cr}, \hat{\theta}_0, \hat{h}]$. For each quantity, the uncertainty associated with the measurement (for ρ) or to the inverse method (for $\hat{\boldsymbol{p}}$) is indicated, with 96% of confidence for the latter.

The influence of the volume fraction V_f of VW on the frequency-dependent ultrasound characteristics is depicted in Fig. 6 for $V_f = 100$, 75, 50 and 0%, recalling that 0% corresponds to the pure soft elastomer, named as EB100. For the readability of the figure, only one out of the three measurements performed on VW100 was arbitrarily chosen, *i.e.*, measurement #1. As expected, the optimized Szabo's parameters $\boldsymbol{p_r}$ are closely related to the volume fraction of VW. Indeed, when the volume fraction of VW decreases (from 100%

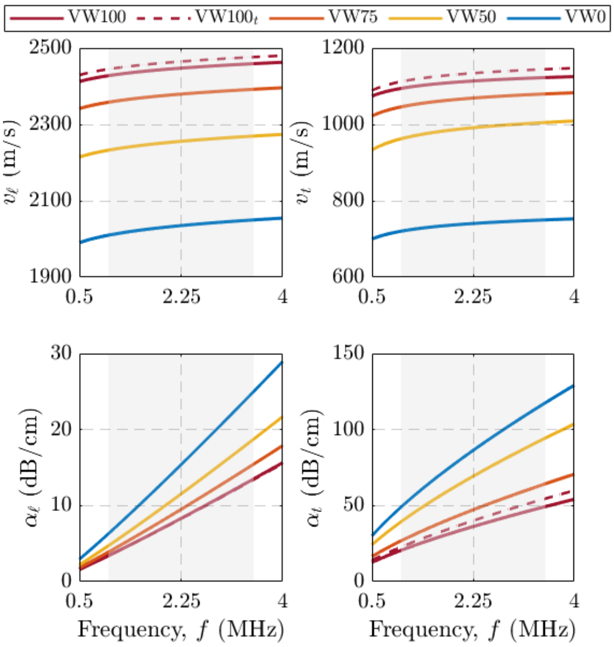

Figure 6: Ultrasound characteristics, *i.e.* the phase velocity $v_r(\omega)$ and the attenuation $\alpha_r(\omega)$, of VW100 (red), VW75 (orange), VW50 (yellow) and EB100 (blue) samples. The light gray areas display the useful frequency bandwidth of the probe on which the inversion was conducted.

to 0%), the phase velocity decreases, and the attenuation increases. In particular, the optimized longitudinal parameters, *i.e.*, $[v_{c\ell}, \alpha_{c\ell}]$, range from [2447 ± 0.2 m/s, 8.31 ± 0.01 dB/cm] for VW100 to [2035.1 ± 0.9 m/s, 15.4 ± 0.03 dB/cm] for EB100 (recall Table 1). A similar trend is observed for the transverse parameters, *i.e.*, $[v_{ct}, \alpha_{ct}]$, with optimized values ranging from [1134.2 ± 0.4 m/s, 40.1 ± 0.1 dB/cm] to [740.6 ± 0.8 m/s, 86.3 ± 1.5 dB/cm]. Overall, it can be observed that the transverse phase velocity v_t is around two to three times lower than v_ℓ depending on the volume fraction of VW.

5.3. Dispersive properties of photopolymer materials

As displayed in Fig. 5, the longitudinal (respectively transverse) phase velocity v_ℓ (respectively v_t) increases of nearly 50 m/s (respectively 40 m/s) over the useful frequency bandwidth (*i.e.*, 0.75–3.75 MHz). Likewise, the longitudinal (respectively transverse) attenuation α_ℓ (respectively α_t) increases from 3 dB/cm to nearly 15 dB/cm (respectively from 12 dB/cm to 70 dB/cm). Interestingly, the dispersion of both the longitudinal and transverse characteristics, which depends on α_{cr} and y_r, is similar for all samples, no matter whether they consist of pure or composite materials (see Fig. 6).

6. Discussion

The objective of the present work was to provide a methodological framework to identify both the frequency-dependent viscoelastic properties in the MHz regime and the thickness of highly attenuating samples. Towards this goal, angular measurements achieved in double through-transmission were conducted on different photopolymer samples, which were obtained using multi-material additive manufacturing. A direct modeling of the double trough-transmission, based on a global matrix formalism, was proposed, along with an inverse procedure, which altogether allowed inferring frequency-dependent ultrasound characteristics.

The proposed framework presents several advantages. First, in contrast to the approach used in [16], the experimental input consisted of the raw temporal signals (i.e., angular measurements) achieved in double through-transmission. Thereby, no signal processing steps were required to isolate the echoes of interest to compute their respective complex spectra, such as signal windowing or phase unwrapping. In addition, the use of a reference signal (*i.e.*, a double through-transmitted signal through water only) allowed weighting the measurements by the input signal bandwidth, thereby preventing any frequency range to be manually selected. A further advantage of using this reference signal was that the distances between the probe, the sample and the mirror could be considered as unknown. Second, the use of global matrix formalism for the modeling of the double through-transmitted signals allowed retrieving temporal θ-scans, which could be systematically compared to the measurements in order to identify the ultrasound characteristics. In addition, the use of a rheological model such as the Szabo's model allowed identifying frequency-dependent properties with a reduced set of model parameters. Third, all the investigated parameters, including both ultrasound characteristics (phase velocity and attenuation of longitudinal and transverse waves) and the sample's thickness were simultaneously optimized. In particular, an original initialization strategy using Prony's series decomposition was proposed, which is based on the measurement achieved in normal incidence. Altogether, this study provides a deeper insight on the ultrasound characteristics of state-of-the-art photopolymers commonly used for polyjet printing purposes, and in particular their transverse properties, which characterization remained challenging for such attenuating materials. To the best of our knowledge, the transverse properties of the soft elastomer (EB) investigated herein have not been reported in the ultrasonic regime so far.

The longitudinal bulk properties of the glassy polymer (VW) and of the soft elastomer (EB) were in good qualitative agreement with those reported in previous studies for photopolymer materials achieved with similar additive manufacturing technologies [9, 16, 10]. Nonetheless, it is not straightforward to quantitatively compare the results of the present work with the literature because (i) the photopolymers may slightly differ across studies (their commercial names change and their compositions are unknown) and (ii) the material properties are not necessarily evaluated in the same frequency range, whereas it has been shown that such photopolymer materials exhibit a frequency-dependent behavior. On the one hand, the longitudinal phase velocity of VW-like samples reported in the literature range from 2464 to 2495 m/s at a central frequency of about 2.25 MHz [10, 15, 16]. Likewise, the values of the longitudinal attenuation of VW reported herein (recall Table 1) is also in close agreement with those of the literature, which range from 7.6 to 8.2 dB/cm [15, 16]. On the other hand, Bakaric et al. [10] reported longitudinal bulk properties close to 2040 m/s and 18.4 dB/cm for Agilus30, which is a soft elastomer similar to ElasticoBlack (EB) used for 3D printing purposes with the Polyjet technology.

In the same way, the transverse bulk properties reported by Gattin et al. [16] for a VW-like sample with a phase velocity of 1112.9±4.5 m/s and attenuation of 37.9±0.5 dB/cm are in very good agreement with those obtained herein (recall Table 1). While the transverse properties of EB have not been reported so far, Gattin et al. [16] investigated a composite material made of VW and an intermediate volume fraction up to 18% of a soft elastomer (TangoBlack™), a photopolymer also used for 3D printing with Polyjet technology. The properties obtained for this material are consistent with our VW75 sample (intermediate volume fraction equal to 25% of EB) with a transverse phase velocity equal to 1066.2±3.7 m/s (VW75: 1069.1±0.2) and an attenuation of 48.8±0.6 dB/cm (VW75: 47.2±0.2 dB/cm).

Overall, the reported properties are all in very good agreement with those of the literature, thereby confirming the robustness of the proposed inverse identification procedure based on ultrasonic angular measurements achieved in double through-transmission. Moreover, the values of the sample thickness concurrently obtained from the optimization are very close to the reference values with less than 5% of relative error, which is consistent with the resolution of the caliper (±0.02mm). Eventually, it is worth mentioning the possible effects of the water -and thus the sample- temperature, which could explain the small discrepancies observed [35]. Despite these promising results, our approach suffers from some limitations. First, some discrepancies were observed over the three measurement repetitions performed on the VW100 samples, as well as between the two VW100 samples with different thicknesses (recall Fig. 5). The inter and intra-sample reproducibilities, which are of the same order of magnitude and lower than 5% for both the phase velocities v_{cr} and attenuations α_{cr}, were significantly higher than the uncertainty associated with the inverse procedure. Such variations may be related to a misalignment of the probe/mirror, or to the parallelism/curvature of the sample, and could be minimized by improving the experimental setup and manufacturing process. Second, the number of investigated samples is relatively low and further composite samples with intermediate volume fractions should be incorporated in future studies, with the aim of establishing mixing rules for these materials in the ultrasonic regime.

Altogether, this study provides an original framework to retrieve the frequency-dependent ultrasound characteristics of dissimilar viscoelastic materials, ranging from glassy polymer to soft elastomer. The properties reported here are of significant interest towards applications requiring a precise knowledge of both the longitudinal and transverse bulk properties of such materials in the MHz regime, as for instance the modeling of the wave interactions with multi-material architectured media [14]. A next step will be to generalize the identification procedure to other kind of polymers and to anisotropic media. In this respect, the use of a phenomenological model to describe the dispersion and attenuation relation will be avoided. To this end, the measurements will be carried out on a larger frequency-range and the inversion will be performed for each frequency. Likewise, the versatility of design at different scales (from micro to macro) offered by multi-material additive manufacturing strengthens the need to account for anisotropy in further works.

7. Author declaration

There are no known conflicts of interest associated with this publication and there has been no significant financial support for this work that could have influenced its outcome. This work was supported by the "Coup de pouce 2022" of the *Fédération Francilienne de Mécanique* (F2M) for young researchers.

8. Data availability

The experimental data as well as the MATLAB script necessary to reproduce the presented method and results are available as an open access repository [36].

References

[1] N. Li, S. Huang, G. Zhang, R. Qin, W. Liu, H. Xiong, G. Shi, J. Blackburn, Progress in additive manufacturing on new materials: A review, J. Mater. Sci. Technol. 35 (2019) 242–269.

[2] A. du Plessis, C. Broeckhoven, I. Yadroitsava, I. Yadroitsev, C. H. Hands, R. Kunju, D. Bhate, Beautiful and Functional: A Review of Biomimetic Design in Additive Manufacturing, Addit. Manuf. 27 (2019) 408–427.

[3] A. Velasco-Hogan, J. Xu, M. A. Meyers, Additive Manufacturing as a Method to Design and Optimize Bioinspired Structures, Adv. Mater. 30 (2018) 1800940.

[4] G. Dong, D. Tessier, Y. F. Zhao, Design of Shoe Soles Using Lattice Structures Fabricated by Additive Manufacturing, Proceedings of the Design Society: International Conference on Engineering Design 1 (2019) 719–728.

[5] Y. Zhang, M.-T. Hsieh, L. Valdevit, Mechanical performance of 3D printed interpenetrating phase composites with spinodal topologies, Compos. Struct. 263 (2021) 113693.

[6] M. J. Mirzaali, M. Cruz Saldívar, A. Herranz de la Nava, D. Gunashekar, M. Nouri-Goushki, E. L. Doubrovski, A. A. Zadpoor, Multi-Material 3D Printing of Functionally Graded Hierarchical Soft–Hard Composites, Adv. Eng. Mater. 22 (2020) 1901142.

[7] A. R. Studart, Additive manufacturing of biologically-inspired materials, Chem. Soc. Rev. 45 (2016) 359–376.

[8] J. Giannatsis, V. Dedoussis, Additive fabrication technologies applied to medicine and health care: A review, Int. J. Adv. Manuf. Technol. 40 (2007) 116–127.

[9] J.-R. Jacquet, F. Ossant, F. Levassort, J.-M. Gregoire, 3-D-Printed Phantom Fabricated by Photopolymer Jetting Technology for High-Frequency Ultrasound Imaging, IEEE Trans. Ultrason. Ferroelectr. Freq. Control 65 (2018) 1048–1055.

[10] M. Bakaric, P. Miloro, A. Javaherian, B. T. Cox, B. E. Treeby, M. D. Brown, Measurement of the ultrasound attenuation and dispersion in 3D-printed photopolymer materials from 1 to 3.5 MHz, J. Acoust. Soc. Am 150 (2021) 2798.

[11] M. Ferri, J. M. Bravo, J. Redondo, S. Jiménez-Gambín, N. Jiménez, F. Camarena, J. V. Sánchez-Pérez, On the Evaluation of the Suitability of the Materials Used to 3D Print Holographic Acoustic Lenses to Correct Transcranial Focused Ultrasound Aberrations, Polymers 11 (2019) 1521.

[12] A. Tikhonov, P. Evdokimov, E. Klimashina, S. Tikhonova, E. Karpushkin, I. Scherbackov, V. Dubrov, V. Putlayev, Stereolithographic fabrication of three-dimensional permeable scaffolds from CaP/PEGDA hydrogel biocomposites for use as bone grafts, J. Mech. Behav. Biomed. Mater. 110 (2020) 103922.

[13] M. Gattin, N. Bochud, G. Rosi, Q. Grossman, D. Ruffoni, S. Naili, Ultrasonic bandgaps in viscoelastic 1D-periodic media: Mechanical modeling and experimental validation, Ultrasonics 131 (2023) 106951.

[14] M. Gattin, N. Bochud, Q. Grossman, D. Ruffoni, G. Rosi, S. Naili, Ultrasound monitoring of multiphase architectured media: Bandgap tracking via the measurement of the reflection coefficient, Appl. Acoust. 217 (2024) 109844.

[15] A. Aghaei, N. Bochud, G. Rosi, Q. Grossman, D. Ruffoni, S. Naili, Ultrasound characterization of bioinspired functionally graded soft-to-hard composites: Experiment and modeling, J. Acoust. Soc. Am. 151 (2022) 1490–1501.

[16] M. Gattin, N. Bochud, G. Rosi, Q. Grossman, D. Ruffoni, S. Naili, Ultrasound characterization of the viscoelastic properties of additively manufactured photopolymer materials, J. Acoust. Soc. Am. 152 (2022) 1901–1912.

[17] S. I. Rokhlin, W. Wang, Double through-transmission bulk wave method for ultrasonic phase velocity measurement and determination of elastic constants of composite materials, J. Acoust. Soc. Am. 91 (1992) 3303–3312.

[18] Y. C. Chu, S. I. Rokhlin, Comparative analysis of through-transmission ultrasonic bulk wave methods for phase velocity measurements in anisotropic materials, J. Acoust. Soc. Am. 95 (1994) 3204–3212.

[19] D. Zhou, L. Peirlinckx, L. Van Biesen, Identification of parametric models for ultrasonic double transmission experiments on viscoelastic plates, J. Acoust. Soc. Am. 99 (1996) 1446–1458.

[20] M. Castaings, B. Hosten, T. Kundu, Inversion of ultrasonic, plane-wave transmission data in composite plates to infer viscoelastic material properties, NDT E Int. 33 (2000) 377–392.

[21] B. Hosten, Reflection and transmission of acoustic plane waves on an immersed orthotropic and viscoelastic solid layer, J. Acoust. Soc. Am. 89 (1991) 2745–2752.

[22] L. Peirlinckx, P. Guillaume, R. Pintelon, L. Van Biesen, A global system identification approach for the accurate parametric modeling of ultrasonic reflection and transmission experiments, IEEE Trans. Ultrason. Ferroelectr. Freq. Control 43 (1996) 628–639.

[23] B. Hosten, M. Castaings, Comments on the ultrasonic estimation of the viscoelastic properties of anisotropic materials, Compos. Part A Appl. Sci. Manuf. 39 (2008) 1054–1058.

[24] A. I. Lavrentyev, S. I. Rokhlin, Determination of elastic moduli, density, attenuation, and thickness of a layer using ultrasonic spectroscopy at two angles, J. Acoust. Soc. Am. 102 (1997) 3467–3477.

[25] E. Siryabe, M. Rénier, A. Meziane, J. Galy, M. Castaings, Apparent anisotropy of adhesive bonds with weak adhesion and non-destructive evaluation of interfacial properties, Ultrasonics 79 (2017) 34–51.

[26] L. Zorzetto, L. Andena, F. Briatico-Vangosa, L. De Noni, J.-M. Thomassin, C. Jérôme, Q. Grossman, A. Mertens, R. Weinkamer, M. Rink, D. Ruffoni, Properties and role of interfaces in multimaterial 3D printed composites, Sci. Rep. 10 (2020) 22285.

[27] D. Royer, E. Dieulesaint, Elastic Waves in Solids I: Free and Guided Propagation, Springer Science & Business Media, 1999.

[28] S. Catheline, J.-L. Gennisson, G. Delon, M. Fink, R. Sinkus, S. Abouelkaram, J. Culioli, Measurement of viscoelastic properties of homogeneous soft solid using transient elastography: An inverse problem approach, J. Acoust. Soc. Am. 116 (2004) 3734–3741.

[29] W. Marczak, Water as a standard in the measurements of speed of sound in liquids, J. Acoust. Soc. Am. 102 (1997) 2776–2779.

[30] P. He, Direct measurement of ultrasonic dispersion using a broadband transmission technique, Ultrasonics 37 (1999) 67–70.

[31] A. H. Nayfeh, The general problem of elastic wave propagation in multilayered anisotropic media, J. Acoust. Soc. Am. 89 (1991) 1521–1531.

[32] T. L. Szabo, J. Wu, A model for longitudinal and shear wave propagation in viscoelastic media, J. Acoust. Soc. Am. 107 (2000) 2437–2446.

[33] M. O'Donnell, E. T. Jaynes, J. G. Miller, Kramers–Kronig relationship between ultrasonic attenuation and phase velocity, J. Acoust. Soc. Am. 69 (1981) 696–701.

[34] S. Guo, M. Rébillat, N. Mechbal, Prediction of frequency and spatially dependent attenuation of guided waves propagating in mounted and unmounted a380 parts made up of anisotropic viscoelastic composite laminates, Struct. Health. Monit. 22 (2023) 1326–1352.

[35] Q. Baudis, T. Valier-Brasier, R. Wunenburger, Thorough ultrasonic rheology of soft, visco-elastic materials: Example of crosslinked Polyurethane elastomer, Ultrasonics 137 (2024) 107166.

[36] P. Margerit, A.-S. Poudrel, iTSCAN, 2024.

Appendix A. Global matrix formalism

In the two fluid subdomains ($|x| > h/2$), the Helmholtz equation governing the pressure field accepts two plane waves solutions corresponding to the forward *incident* $a_{\mathtt{I}}$ and *transmitted* $a_{\mathtt{T}} \equiv a_0^+$ waves with $\xi_{\mathtt{I}} = \xi_{\mathtt{T}} = \chi_0$ and the backward *reflected* wave $a_{\mathtt{R}} \equiv a_0^-$ with $\xi_{\mathtt{R}} = -\chi_0$ (see Eq. (7)). In the isotropic solid subdomain ($|x| < h/2$), the 2D Navier-Cauchy equations apply which accept 2 solution pairs of backward and forward waves defined by $\xi_r = \pm\chi_r$ and corresponding to *longitudinal* ($r = \ell$) and *transverse* ($r = t$)

motion associated, respectively, with:

$$k_\ell^2 = \chi_\ell^2 + \kappa^2 = \omega^2 \, \frac{\rho}{\lambda + 2\mu} \quad , \quad \boldsymbol{\mathcal{U}}^{(\ell)} = \frac{1}{\omega^2} \begin{bmatrix} \xi_r \\ \kappa \end{bmatrix} \tag{A.1a}$$

$$k_t^2 = \chi_t^2 + \kappa^2 = \omega^2 \, \frac{\rho}{\mu} \quad , \quad \boldsymbol{\mathcal{U}}^{(t)} = \frac{1}{\omega^2} \begin{bmatrix} -\kappa \\ \xi_r \end{bmatrix} \tag{A.1b}$$

where (λ, μ) are the Lamé coefficients and the scaling of the wave polarization vectors $\boldsymbol{\mathcal{U}}^{(r)}$ with ω has been introduced to simplify the derivations. Using Hooke's law to express the local stress vector as a function of the elementary waves in the solid, the 6 continuity equations in Eq. (5) (3 equations on 2 interfaces) can be recast as the following system:

$$\sum_{r=\{0,\ell,t\}} \left(\begin{bmatrix} z_r \boldsymbol{\mathcal{B}}^{(r^+)} & z_r^{-1} \boldsymbol{\mathcal{B}}^{(r^-)} \\ z_r^{-1} \boldsymbol{\mathcal{B}}^{(r^+)} & z_r \boldsymbol{\mathcal{B}}^{(r^-)} \end{bmatrix} \begin{bmatrix} a_r^+ \\ a_r^- \end{bmatrix} \right) = -a_{\mathtt{I}} \begin{bmatrix} z_0 \boldsymbol{\mathcal{B}}^{(0^+)} \\ \mathbf{0} \end{bmatrix} \tag{A.2}$$

$$\boldsymbol{\mathcal{B}}^{(r)} = \begin{bmatrix} \rho\,\omega^2 \left[\xi_r k_t^2 \, \mathcal{U}_1^{(r)} + \kappa (k_t^2 - 2k_\ell^2) \, \mathcal{U}_2^{(r)} \right] + \mathrm{i} k_\ell^2 \, k_t^2 \, \mathcal{P}^{(r)} \\ \rho\,\omega^2 \, k_\ell^2 \left(\kappa \, \mathcal{U}_1^{(r)} + \xi_r \, \mathcal{U}_2^{(r)} \right) \\ \rho_0 \, \omega^2 \, \mathcal{U}_1^{(r)} + \mathrm{i} \xi_r \, \mathcal{P}^{(r)} \end{bmatrix}$$

where $z_r = e^{\mathrm{i} \frac{h}{2} \chi_r}$. Notice that $a_{\mathtt{I}}$, as the source term, has been placed in the right-hand side. The symmetry of the forward–backward waves (given by $\xi_r = \pm \chi_r$) and the symmetry of the solid–fluid interfaces (located at $x = \pm h/2$) are taken into account by the change of variables $a_r^\pm = a_r^S \pm a_r^A$, the use of $c_r = \cos \frac{h}{2} \chi_r$ and $s_r = \sin \frac{h}{2} \chi_r$ and the vectors $\boldsymbol{\mathcal{S}}^{(r)} = \boldsymbol{\mathcal{B}}^{(r^+)} + \boldsymbol{\mathcal{B}}^{(r^-)}$ and $\boldsymbol{\mathcal{A}}^{(r)} = \boldsymbol{\mathcal{B}}^{(r^+)} - \boldsymbol{\mathcal{B}}^{(r^-)}$ with few non-zero coefficients:

$$\mathcal{S}_1^{(0)} = 2\mathrm{i} \, (\chi_t^2 + \kappa^2) \ , \ \mathcal{A}_3^{(0)} = 2\mathrm{i} \, \chi_0$$

$$\mathcal{S}_1^{(\ell)} = \mathcal{S}_2^{(t)} = 2\rho(\chi_t^2 - \kappa^2) \ , \ \mathcal{S}_3^{(t)} = -2\rho_0 \, \kappa$$

$$\mathcal{A}_1^{(t)} = -4\rho \, \kappa \, \chi_t \ , \ \mathcal{A}_2^{(\ell)} = 4\rho \, \kappa \, \chi_\ell \ , \ \mathcal{A}_3^{(\ell)} = 2\rho_0 \, \chi_\ell$$

Altogether, this allows rewriting Eq. (A.2) as two smaller systems of uncoupled equations:

$$\begin{bmatrix} z_0^{-1}\,\mathcal{S}_1^{(0)} & 2c_\ell\,\mathcal{S}_1^{(\ell)} & 2c_t\,\mathcal{A}_1^{(t)} \\ 0 & 2s_\ell\,\mathcal{A}_2^{(\ell)} & 2s_t\,\mathcal{S}_2^{(t)} \\ \mathrm{i}z_0^{-1}\,\mathcal{A}_3^{(0)} & 2s_\ell\,\mathcal{A}_3^{(\ell)} & 2s_t\,\mathcal{S}_3^{(t)} \end{bmatrix} \begin{bmatrix} a_0^S \\ a_\ell^S \\ a_t^A \end{bmatrix} = \begin{bmatrix} -z_0\,\mathcal{B}_1^{(0^+)} \\ 0 \\ \mathrm{i}z_0\,\mathcal{B}_3^{(0^+)} \end{bmatrix} a_\mathrm{I} \tag{A.3}$$

$$\begin{bmatrix} -\mathrm{i}z_0^{-1}\,\mathcal{S}_1^{(0)} & 2s_\ell\,\mathcal{S}_1^{(\ell)} & 2s_t\,\mathcal{A}_1^{(t)} \\ 0 & 2c_\ell\,\mathcal{A}_2^{(\ell)} & 2c_t\,\mathcal{S}_2^{(t)} \\ z_0^{-1}\,\mathcal{A}_3^{(0)} & 2c_\ell\,\mathcal{A}_3^{(\ell)} & 2c_t\,\mathcal{S}_3^{(t)} \end{bmatrix} \begin{bmatrix} a_0^A \\ a_\ell^A \\ a_t^S \end{bmatrix} = \begin{bmatrix} -\mathrm{i}z_0\,\mathcal{B}_1^{(0^+)} \\ 0 \\ -z_0\,\mathcal{B}_3^{(0^+)} \end{bmatrix} a_\mathrm{I} \tag{A.4}$$

that can be inverted in order to finally obtain:

$$a_0^S = \frac{z_0^2}{2}\,a_\mathrm{I}\,\frac{(\alpha\,c_\ell\,s_t + \beta\,s_\ell\,c_t) - \mathrm{i}\gamma\,s_\ell\,s_t}{(\alpha\,c_\ell\,s_t + \beta\,s_\ell\,c_t) + \mathrm{i}\gamma\,s_\ell\,s_t} \tag{A.5}$$

$$a_0^A = \frac{z_0^2}{2}\,a_\mathrm{I}\,\frac{\gamma\,c_\ell\,c_t - \mathrm{i}(\alpha\,s_\ell\,c_t + \beta\,c_\ell\,s_t)}{\gamma\,c_\ell\,c_t + \mathrm{i}(\alpha\,s_\ell\,c_t + \beta\,c_\ell\,s_t)} \tag{A.6}$$

where α, β and γ are given in Eq. (9).

Appendix B. Initialization

The expression of the inverse double-transmitted wave transfer given in Eq. (14) is an harmonic polynomial which poles $(\psi_\ell^{-\omega}, 1, \psi_\ell^{\omega})$ can be estimated after compensation of the water-related phase ψ_0^{ω}. More particularly, it is well-known from Prony's works that the data samples $h_n = \psi_0^{-\omega} H_{2\mathrm{T}}^{-1}(n\Delta\omega)$ are related by the following recurrence relation:

$$0 = h_{n+3} + \sum_{m=0}^{2} p_m\,h_{n+m} \tag{B.1}$$

and that the roots of the polynomial $P(\pi)$ formed by the coefficients p_m are the signal poles:

$$P(\pi) = \pi^3 + \sum_{m=0}^{2} p_m\,\pi^m = (\pi - \psi_\ell^{-\Delta\omega})(\pi - 1)(\pi - \psi_\ell^{\Delta\omega}) \tag{B.2}$$

Hence the recurrence relation takes the following form:

$$(h_{n+3} - h_n) - p_2(h_{n+2} - h_{n+1}) = 0 \tag{B.3}$$

$$p_2 = (\psi_\ell^{\Delta\omega} + \psi_\ell^{-\Delta\omega} + 1) = 2\cos\frac{2h\Delta\omega}{v_\ell} + 1 \tag{B.4}$$

The coefficient p_2 can be estimated from the normal incidence data $\boldsymbol{h} = [h_1 \ \ldots \ h_N]$ using weighted least-squares, the chosen weight taking into account the input signal bandwidth. At the end, the initial frequency-independent longitudinal wave speed is obtained as:

$$v_\ell = \frac{2h\Delta\omega}{\mathrm{acos}\left(\frac{p_2 - 1}{2}\right)} \tag{B.5}$$